



Global and Spatial Compartmental Interrelationships of Bone Density, Microstructure, Geometry and Biomechanics in the Distal Radius in a Colles' Fracture Study Using HR-pQCT

OPEN ACCESS

Kazuteru Shiraishi^{1,2}, Andrew J. Burghardt³, Makoto Osaki², Sundeep Khosla⁴ and Julio Carballido-Gamio^{1*}

Edited by:

Karupppasamy Subburaj,
Singapore University of Technology
and Design, Singapore

Reviewed by:

Anitha D. Praveen,
Singapore University of Technology
and Design, Singapore
Muthu Rama Krishnan Mookiah,
University of Dundee, United Kingdom

*Correspondence:

Julio Carballido-Gamio
Julio.Carballido-Gamio@
cuanschutz.edu

Specialty section:

This article was submitted to
Bone Research,
a section of the journal
Frontiers in Endocrinology

Received: 01 June 2020

Accepted: 01 April 2021

Published: 26 May 2021

Citation:

Shiraishi K, Burghardt AJ, Osaki M,
Khosla S and Carballido-Gamio J
(2021) Global and Spatial
Compartmental Interrelationships of
Bone Density, Microstructure,
Geometry and Biomechanics in the
Distal Radius in a Colles' Fracture
Study Using HR-pQCT.
Front. Endocrinol. 12:568454.
doi: 10.3389/fendo.2021.568454

¹ Department of Radiology, University of Colorado Anschutz Medical Campus, Aurora, CO, United States, ² Department of Orthopedic Surgery, Nagasaki University Graduate School of Biomedical Sciences, Nagasaki, Japan, ³ Department of Radiology and Biomedical Imaging, University of California, San Francisco, San Francisco, CA, United States, ⁴ Division of Endocrinology, Diabetes, Metabolism and Nutrition, Department of Internal Medicine, College of Medicine, Mayo Clinic, Rochester, MN, United States

Background: Bone parameters derived from HR-pQCT have been investigated on a parameter-by-parameter basis for different clinical conditions. However, little is known regarding the interrelationships of bone parameters and the spatial distribution of these interrelationships. In this work: 1) we investigate compartmental interrelationships of bone parameters; 2) assess the spatial distribution of interrelationships of bone parameters; and 3) compare interrelationships of bone parameters between postmenopausal women with and without a recent Colles' fracture.

Methods: Images from the unaffected radius in fracture cases (n=84), and from the non-dominant radius of controls (n=98) were obtained using HR-pQCT. Trabecular voxel-based maps of local bone volume fraction (L.Tb.BV/TV), homogenized volumetric bone mineral density (H.Tb.BMD), homogenized μ FEA-derived strain energy density (H.Tb.SED), and homogenized inter-trabecular distances (H.Tb.1/N) were generated; as well as surface-based maps of apparent cortical bone thickness (Surf.app.Ct.Th), porosity-weighted cortical bone thickness (Surf.Ct.SIT), mean cortical BMD (Surf.Ct.BMD), and mean cortical SED (Surf.Ct.SED). Anatomical correspondences across the parametric maps in the study were established *via* spatial normalization to a common template. Mean values of the parametric maps before spatial normalization were used to assess compartmental Spearman's rank partial correlations of bone parameters (e.g., between H.Tb.BMD and L.Tb.BV/TV or between Surf.Ct.BMD and Surf.app.Ct.Th). Spearman's rank partial correlations were also assessed for each voxel and vertex of the

spatially normalized parametric maps, thus generating maps of Spearman's rank partial correlation coefficients. Correlations were performed independently within each group, and compared between groups using the Fisher's Z transformation.

Results: All within-group global trabecular and cortical Spearman's rank partial correlations were significant; and the correlations of H.Tb.BMD–L.Tb.BV/TV, H.Tb.BMD–H.Tb.1/N, L.Tb.BV/TV–H.Tb.1/N, Surf.Ct.BMD–Surf.Ct.SED and Surf.Ct.SIT–Surf.Ct.SED were significantly different between controls and fracture cases. The spatial analyses revealed significant heterogeneous voxel- and surface-based correlation coefficient maps across the distal radius for both groups; and the correlation maps of H.Tb.BMD–L.Tb.BV/TV, H.Tb.BMD–H.Tb.1/N, L.Tb.BV/TV–H.Tb.1/N, H.Tb.1/N–H.Tb.SED and Surf.app.Ct.Th - Surf.Ct.SIT yielded small clusters of significant correlation differences between groups.

Discussion: The heterogeneous spatial distribution of interrelationships of bone parameters assessing density, microstructure, geometry and biomechanics, along with their global and local differences between controls and fracture cases, may help us further understand different bone mechanisms of bone fracture.

Keywords: Colles' fracture, HR-pQCT (high-resolution peripheral quantitative computed tomography), bone, interrelationships, spatial analysis

INTRODUCTION

Osteoporosis is defined as a skeletal disorder characterized by compromised bone strength predisposing a person to an increased risk of fracture (1). Bone strength depends on both bone mineral density (BMD) and bone quality, which includes factors such as bone microstructure, micro fracture, bone turnover, and mineralization (1). Therefore, areal BMD (aBMD) derived from dual energy X-ray absorptiometry (DXA), which is the clinical standard for osteoporosis assessment, provides a limited evaluation of bone strength (2). This limitation has been manifested with non-osteoporotic subjects (T-score > -2.5) sustaining fragility fractures (3, 4). Consequently, additional assessments such as volumetric BMD (BMD) and quantification of the trabecular and cortical bone microstructure and geometry, might improve the prevention of fragility fractures (5–8).

High-resolution peripheral quantitative computed tomography (HR-pQCT) enables *in vivo* visualization of the three-dimensional (3D) bone microstructure at the distal radius and tibia with high spatial resolution and a low level of radiation exposure (9, 10). Because of its small voxel size (82 μm isotropic; 61 μm isotropic in the second-generation scanner), this unique medical imaging modality can distinguish between cortical and trabecular bone, and allows 3D assessments of microstructure, density, and geometry. In addition, HR-pQCT provides the capability of estimating bone strength using micro-finite element analysis (μFEA) (11, 12). Since the introduction of this high-resolution imaging modality, many studies have been performed to evaluate the effectiveness of several bone microstructural features in the assessment of various bone disorders (13).

Colles' fracture is the most common fragility fracture in the distal radius, with osteoporosis being a risk factor, especially for postmenopausal women (14). Existing studies using HR-pQCT have demonstrated that lower BMD and deterioration of bone microstructure and geometry in the cortical and trabecular bone compartments are associated with fragility fractures in postmenopausal women (5–7, 11, 15–17), particularly for wrist fracture (12, 16, 18, 19). However, although it is known that density, quality of bone microstructure, geometry, and bone strength estimates derived from μFEA are significantly correlated (15), it is unknown how these associations are affected in subjects sustaining fragility fractures. Furthermore, it is unknown if these associations are spatially homogeneous, even in healthy subjects. We hypothesize that in subjects with a recent Colles' fracture, there is a disruption in the interrelationship of bone parameters. The purpose of this work was then to investigate interrelationships of bone parameters in postmenopausal women with and without a recent Colles' fracture to help our understanding of potential mechanisms of bone fracture using HR-pQCT. In particular, interrelationships of density, microstructural, geometrical and biomechanical parameters derived from μFEA were investigated globally and spatially for both the trabecular and cortical bone compartments.

METHODS

Subjects

This work was based on existing data from the study of Melton et al. (18). Recruited subjects were 100 postmenopausal women newly diagnosed with a Colles' fracture in Olmsted

County, Minnesota; and 105 postmenopausal controls frequency-matched based on the expected age distribution of forearm fractures in that community. The event that precipitated the fracture was characterized according to the scheme of Palvanen and colleagues (20). Controls had no history of another osteoporotic fracture that occurred after age 35 years.

This research was conducted in accordance to the regulations of the participating institutions and informed consent was obtained from all participants prior to enrollment. Analyses were performed based on de-identified data.

Imaging

Imaging of the distal radius for each subject was performed using an HR-pQCT system (XtremeCT; Scanco Medical AG, Brüttisellen, Switzerland). The forearm was fixed in a carbon fiber cast, then inserted into the gantry of the scanner. The non-dominant side in controls and the unaffected side in fracture cases was scanned. The starting point of the fixed scan region was 9.5 mm proximal from a reference line set manually at the endplate in the distal radius. Scan settings were as follows: voltage 60 kVp, current 900 μ A, integration time 100 ms, and effective dose 4.2 μ Sv. A 9.02 mm section spanned by a total of 110 slices was imaged with an isotropic voxel size of 82 μ m. Subjects were rescanned if clear images were not obtained. For this study, all scans were scored for presence and severity of motion artifacts using the current artifact grading scheme of the manufacturer (21). Grades are based on the appearance of horizontal streakings, contiguity of cortical bone, and amount of trabecular smearing. Grade 1 represents no motion artifacts, Grade 2 minor motion artifacts, Grade 3 moderate motion artifacts, and Grades 4 and 5 represent severe and extreme motion artifacts, respectively. Only scans with image quality scores of 1 to 3 were analyzed in this work. **Figure 1** shows

representative axial cross-sections of HR-pQCT scans of the distal radius for three controls and three fracture cases.

Image Analysis

Standard Analysis

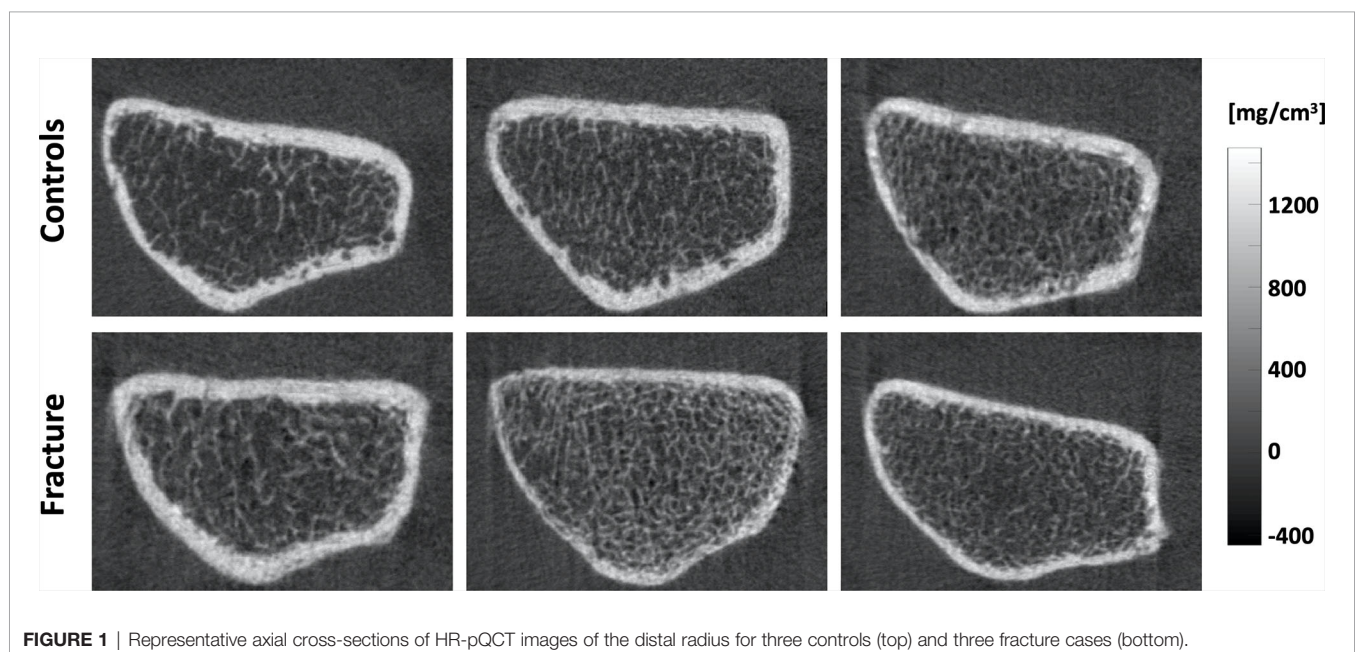
Bone segmentation from HR-pQCT images was performed using the standard evaluation software provided by the manufacturer as mentioned in other studies (22, 23). Briefly, the periosteal contours of the distal radius were identified semi-automatically using an edge-finding algorithm, checked visually, and modified manually as necessary (24). Then, a threshold-based algorithm was used to segment the cortical and trabecular bone compartments enabling compartment-specific assessments of density, microstructure, geometry, and biomechanics (25).

The following parameters were measured for the trabecular and cortical bone compartments: trabecular BMD (Tb.BMD), trabecular bone volume fraction (Tb.BV/TV), trabecular number (Tb.N), trabecular separation (Tb.Sp), cortical BMD (Ct.BMD), and cortical thickness (Ct.Th) (26).

In addition, assessment of apparent biomechanical parameters was accomplished using linear μ FEA as previously described in the literature (27). Briefly, a mesh of isotropic elements was generated from the voxel-based representation of trabecular and cortical bone. Elements in this mesh were assigned an elastic modulus of 6.829 GPa and a Poisson ratio of 0.3. Using the iterative solver provided by the manufacturer, reaction forces on the superior and inferior ends of the model were then calculated for a 1% axial compression. Based on these estimates, failure load (μ FEA.FL) and bone stiffness (μ FEA.Stiffness) were computed as in Mueller et al. (27).

Spatial Analysis

To incorporate parameters assessing bone microstructure and biomechanics in our spatial analyses, we generated maps



representing inter-trabecular distances (Tb.1/N) and μ FEA-derived strain energy density (SED; J/mm^3). SED is defined as the potential energy stored in a volume by virtue of an elastic deformation (18). Then to obtain smooth maps of bone parameters suitable for voxel-wise associations at the population level, we generated homogenized maps of BMD, Tb.1/N and SED, as well as maps representing local assessments of bone volume fraction using spherical kernels ($r=11$ for BMD, SED and BV/TV; $r=5$ for Tb.1/N) (28).

Periosteal surface-based maps encoding the local apparent cortical bone thickness (Surf.app.Ct.Th), effective cortical bone thickness taking into account porosity and partial volume effects (Surf.Ct.SIT; streamline integral thickness), mean cortical BMD (Surf.Ct.BMD), and mean cortical SED (Surf.Ct.SED) at each vertex were also generated as previously described by Carballido-Gamio et al. enabling population-based vertex-wise associations of cortical bone parameters (28). For this purpose, the cortical compartment was identified with an in-house implementation of a non-local fuzzy c-means (NL-FCM) algorithm using BMD maps, bone segmentations, and distances to the periosteal surfaces as clustering features (28). Then, soft cortical bone classification was performed using a fuzzy s-shaped membership function assigning to each voxel a value between 0 (no cortical bone) and 1 (cortical bone) (29), indicating the degree of membership of a voxel to the category of cortical bone (Figure 2). Using the Laplace's equation approach, streamlines providing one-to-one correspondence

without crossings between the periosteal and the endosteal surfaces were computed. The lengths of these streamlines represent the Surf.app.Ct.Th, while the integrals of the soft cortical bone classifications along the trajectories of the streamlines from the periosteal to the endosteal surfaces represent the Surf.Ct.SIT. The mean of BMD and SED values along the trajectories of the streamlines represent the Surf.Ct.BMD and Surf.Ct.SED, respectively.

The smooth voxel-based and the surface-based parametric maps described above were then spatially normalized to a common template of the distal radius as previously described (28). This spatial normalization step established anatomical correspondences across the parametric maps of all subjects in the study enabling the evaluation of voxel-wise and vertex-wise interrelationships of bone parameters. The voxel-based spatially-normalized maps were eroded to avoid the cortical bone and generate spatially-normalized maps of: 1) homogenized Tb.BMD (H.Tb.BMD), 2) homogenized Tb.1/N (H.Tb.1/N), 3) homogenized Tb.SED (H.Tb.SED), and 4) local Tb.BV/TV (L.Tb.BV/TV).

Statistical Analysis

Standard Analysis

Mean values of parameters of bone density, microstructure, geometry and biomechanics were compared between controls and fracture cases with linear regression models adjusting for age, height, and weight.

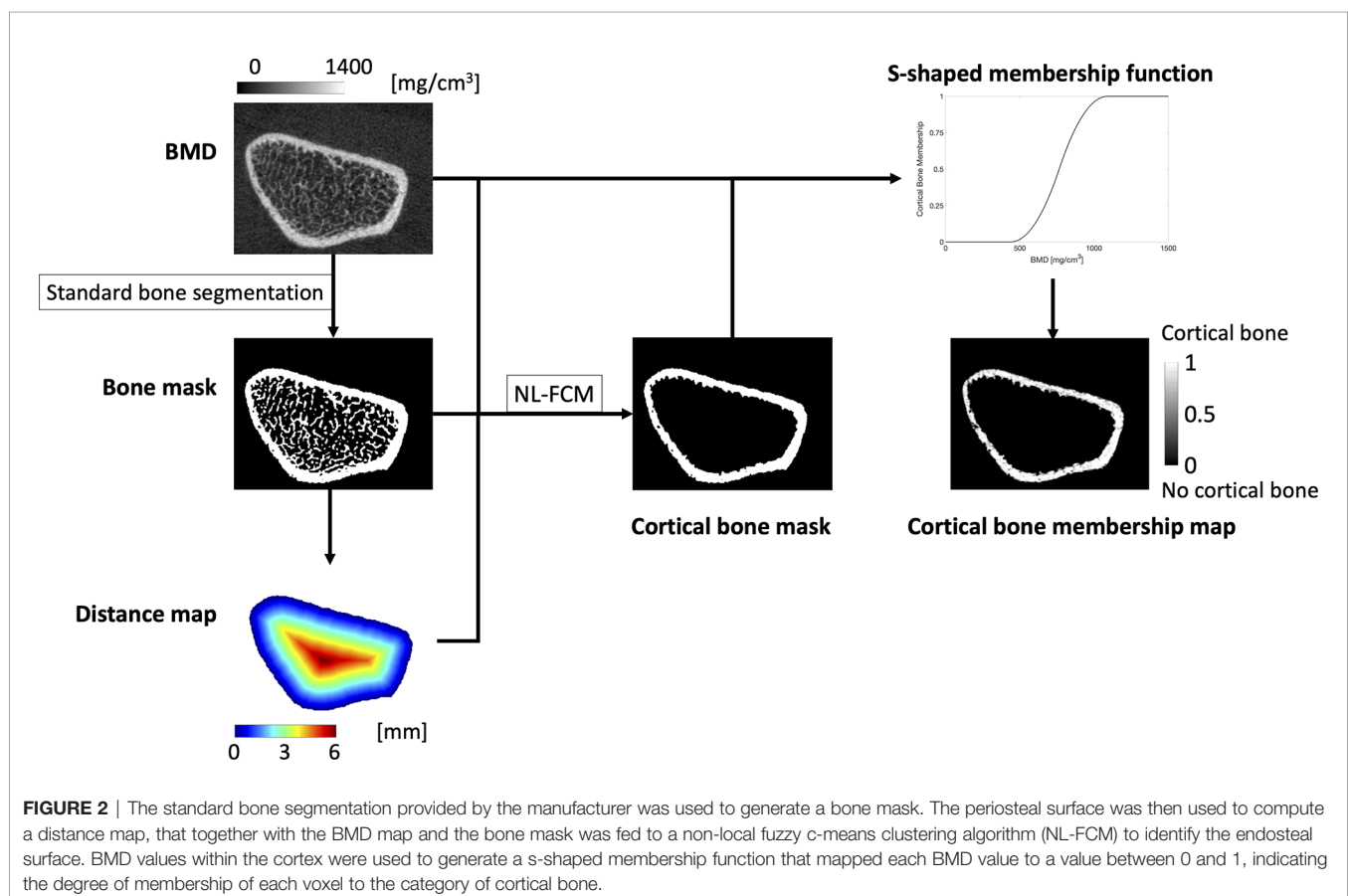


FIGURE 2 | The standard bone segmentation provided by the manufacturer was used to generate a bone mask. The periosteal surface was then used to compute a distance map, that together with the BMD map and the bone mask was fed to a non-local fuzzy c-means clustering algorithm (NL-FCM) to identify the endosteal surface. BMD values within the cortex were used to generate a s-shaped membership function that mapped each BMD value to a value between 0 and 1, indicating the degree of membership of each voxel to the category of cortical bone.

For each compartment, within-group interrelationships of bone parameters were then evaluated using Spearman's rank partial correlations adjusting for age, height and weight. These correlation coefficients were then compared between controls and fracture cases using the Fisher's Z transformation.

P-values in these statistical tests were considered significant if they were less than 0.05.

Spatial Analysis

To assess within-group spatial interrelationships of bone parameters, trabecular voxel-wise and cortical vertex-wise Spearman's rank partial correlations adjusted for age, height, weight, and shape (90% of variance = first 4 principal components) were computed using the spatially-normalized parametric maps. This step generated correlation coefficient maps and their corresponding *P*-value maps in the template space. Given the large number of correlations, *P*-value maps were corrected for multiple comparisons using the false discovery rate method (FDR; $q=0.05$) (30). Spatial comparisons of the correlation coefficients between controls and fracture cases were then performed with voxel-wise and vertex-wise Fisher's Z transformations generating *P*-value maps that were also corrected for multiple comparisons using FDR ($q = 0.05$).

To better understand the spatial correlations, we also performed statistical analyses of the smooth voxel-based maps of trabecular parameters and the surface-based maps of cortical parameters with no spatial normalization. In particular, we: 1) compared mean parametric values between controls and cases using linear regression models adjusting for age, height, and weight; 2) performed within-group Spearman's rank partial correlations of bone parameters within each compartment adjusting for age, height and weight; 3) performed within-

group Spearman's rank partial correlations of bone parameters with μ FEA.FL within each compartment adjusting for age, height and weight; and 4) compared the correlation coefficients between controls and fracture cases using Fisher's Z transformations. *P*-values in these statistical tests were considered significant if they were less than 0.05.

RESULTS

Subject Characteristics

The characteristics of the subjects included in this study are shown in **Table 1**. Twenty-three scans out of 205 were excluded because of severe motion artifacts (grade > 3). Therefore, 182 post-menopausal women were included in the analysis: 98 controls and 84 with a newly diagnosed Colles' fracture. Controls and fracture cases showed no significant differences in age, height, and weight (all $p > 0.05$).

Standard Analysis

Global Comparisons

The differences between groups in BMD, bone microstructure, geometry and μ FEA parameters are summarized in **Table 2**. Subjects with fracture had significantly lower Tb.BMD, Tb.BV/TV, Tb.N, Ct.BMD and Ct.Th (all $p < 0.01$), and significantly higher Tb.Sp ($p = 0.015$) than controls. In addition, the fracture cases had significantly lower μ FEA.FL and μ FEA.Stiffness than controls (both $p < 0.001$).

Global Correlations

All the interrelationships of trabecular and cortical bone parameters were significant within each group ($p < 0.001$), but

TABLE 1 | Subject characteristics.

	Controls	Fracture cases	<i>p</i> -value
Number	98	84	
Age (years)	65.3 ± 9.3	63.8 ± 9.3	NS
Height (cm)	161.2 ± 5.6	161.8 ± 5.7	NS
Weight (kg)	73.6 ± 13.8	74.4 ± 17.7	NS

Values are shown as mean ± standard deviation.

Two-sample *t*-test.

NS = $P \geq 0.05$.

TABLE 2 | Bone parameters assessed with the standard analysis method.

Parameter (units)	Controls	Fracture cases	<i>p</i> -value
Tb.BMD (mg/cm ³)	144.6 ± 39.6	121.1 ± 39.3	<0.001*
Tb.BV/TV	0.23 ± 0.05	0.19 ± 0.05	<0.001*
Tb.N (1/mm)	1.67 ± 0.36	1.47 ± 0.38	<0.001*
Tb.Sp (mm)	0.64 ± 0.30	0.74 ± 0.26	0.015*
Ct.BMD (mg/cm ³)	886.0 ± 73.0	858.4 ± 76.1	<0.001*
Ct.Th (mm)	1.01 ± 0.22	0.95 ± 0.19	<0.01*
μ FEA.FL (N)	2539.3 ± 467.1	2285.0 ± 492.9	<0.001*
μ FEA.Stiffness (N/mm)	44070.2 ± 8425.7	39799.0 ± 8675.9	<0.001*

Values are shown as mean ± standard deviation.

Linear regression adjusting for age, height, and weight.

*Significant at $p < 0.05$.

only the interrelationship of Tb.BMD-Tb.N was significantly different between controls and fracture cases ($p < 0.05$) as shown in **Table 3**.

Spatial Analysis

Statistical Maps

The Spearman's rank partial correlation coefficient maps for the different interrelationships of trabecular bone parameters are shown in **Figure 3** for both controls and fracture cases. These maps revealed significant heterogeneous spatial distributions of correlation coefficients across the distal radius, particularly with stronger correlations proximally than distally in both groups. In addition, in most of the correlation maps, fracture cases showed stronger correlations than controls, which was manifested with clusters of significant different correlation coefficients as shown in **Figure 4** for H.Tb.BMD-L.Tb.BV/TV, H.Tb.BMD-H.Tb.1/N, L.Tb.BV/TV-H.Tb.1/N, and H.Tb.1/N-H.Tb.SED.

Cortical Spearman's rank partial correlation coefficient maps are depicted in **Figure 5** for both controls and fracture cases. These maps also revealed significant heterogeneous distributions of correlation coefficients across the distal radius within each group. However, these heterogeneous distributions were not significantly different between controls and fracture cases, except for the correlation of Suf.app.Ct.Th-Surf.Ct.SIT as is shown in **Figure 6**.

Global Comparisons

Differences in homogenized and local trabecular voxel-based parameters, and in cortical surface-based parameters with no spatial normalization are summarized in **Table 4**. Fracture cases had significantly lower H.Tb.BMD, L.Tb.BV/TV, H.Tb.SED, Surf.Ct.BMD, Surf.app.Ct.Th and Surf.Ct.SIT than controls (all $p < 0.001$). Fracture cases also showed significantly higher

H.Tb.1/N than controls ($p < 0.05$). However, Surf.Ct.SED did not differ between groups.

Global Correlations

The interrelationships of homogenized and local trabecular voxel-based parameters, and cortical surface-based parameters with no spatial normalization using Spearman's rank partial correlations are summarized in **Table 5**. With the exception of the correlation of H.Tb.1/N-H.Tb.SED for controls ($p = 0.006$), all within-group compartmental trabecular and cortical Spearman's rank partial correlations were significant at $p < 0.001$. In addition, the correlations of H.Tb.BMD-L.Tb.BV/TV, H.Tb.BMD-H.Tb.1/N, L.Tb.BV/TV-H.Tb.1/N, Surf.Ct.BMD-Surf.Ct.SED, and Surf.Ct.SIT-Surf.Ct.SED were significantly different between groups at $p < 0.05$.

In terms of correlations with μ FEA.FL, mean values of the homogenized and local trabecular voxel-based parameters and cortical surface-based parameters manifested significant correlations in both groups, except for Ct.SED in the fracture group. There were no significant differences in the strength of these correlations between groups (**Table 6**).

DISCUSSION

In this study, we assessed the spatial distribution of interrelationships of parameters of bone density, microstructure, geometry and biomechanics in the distal radius of postmenopausal women with and without a recent Colles' fracture using HR-pQCT. Spearman's rank partial correlation coefficient maps showed significant heterogeneous spatial distributions of these interrelationships across the distal radius for both groups. In addition, small clusters of significant different interrelationships

TABLE 3 | Global compartmental Spearman's rank partial correlations for bone parameters assessed with the standard analysis method.

Interrelationships		Controls		Fracture cases		Controls vs. Fracture cases
		ρ	p -value	ρ	p -value	p -value
Tb.BMD	Tb.BV/TV	0.98	<0.001*	0.99	<0.001*	NS
Tb.BMD	Tb.N	0.83	<0.001*	0.91	<0.001*	0.03*
Tb.BMD	Tb.Sp	-0.86	<0.001*	-0.91	<0.001*	NS
Tb.BMD	μ FEA.FL	0.67	<0.001*	0.65	<0.001*	NS
Tb.BMD	μ FEA.Stiffness	0.62	<0.001*	0.60	<0.001*	NS
Tb.BV/TV	Tb.N	0.85	<0.001*	0.91	<0.001*	NS
Tb.BV/TV	Tb.Sp	-0.88	<0.001*	-0.92	<0.001*	NS
Tb.BV/TV	μ FEA.FL	0.65	<0.001*	0.65	<0.001*	NS
Tb.BV/TV	μ FEA.Stiffness	0.58	<0.001*	0.59	<0.001*	NS
Tb.N	Tb.Sp	-0.99	<0.001*	-0.99	<0.001*	NS
Tb.N	μ FEA.FL	0.48	<0.001*	0.59	<0.001*	NS
Tb.N	μ FEA.Stiffness	0.40	<0.001*	0.54	<0.001*	NS
Tb.Sp	μ FEA.FL	-0.51	<0.001*	-0.59	<0.001*	NS
Tb.Sp	μ FEA.Stiffness	-0.43	<0.001*	-0.55	<0.001*	NS
μ FEA.FL	μ FEA.Stiffness	0.99	<0.001*	0.99	<0.001*	NS
Ct.BMD	Ct.Th	0.69	<0.001*	0.63	<0.001*	NS

ρ = Spearman's rank partial correlation coefficient.

Spearman's rank partial correlations were adjusted for age, height and weight.

The Fisher's Z transformation was used to compare correlation coefficients between groups.

*Significant at $p < 0.05$.

NS = $P \geq 0.05$.

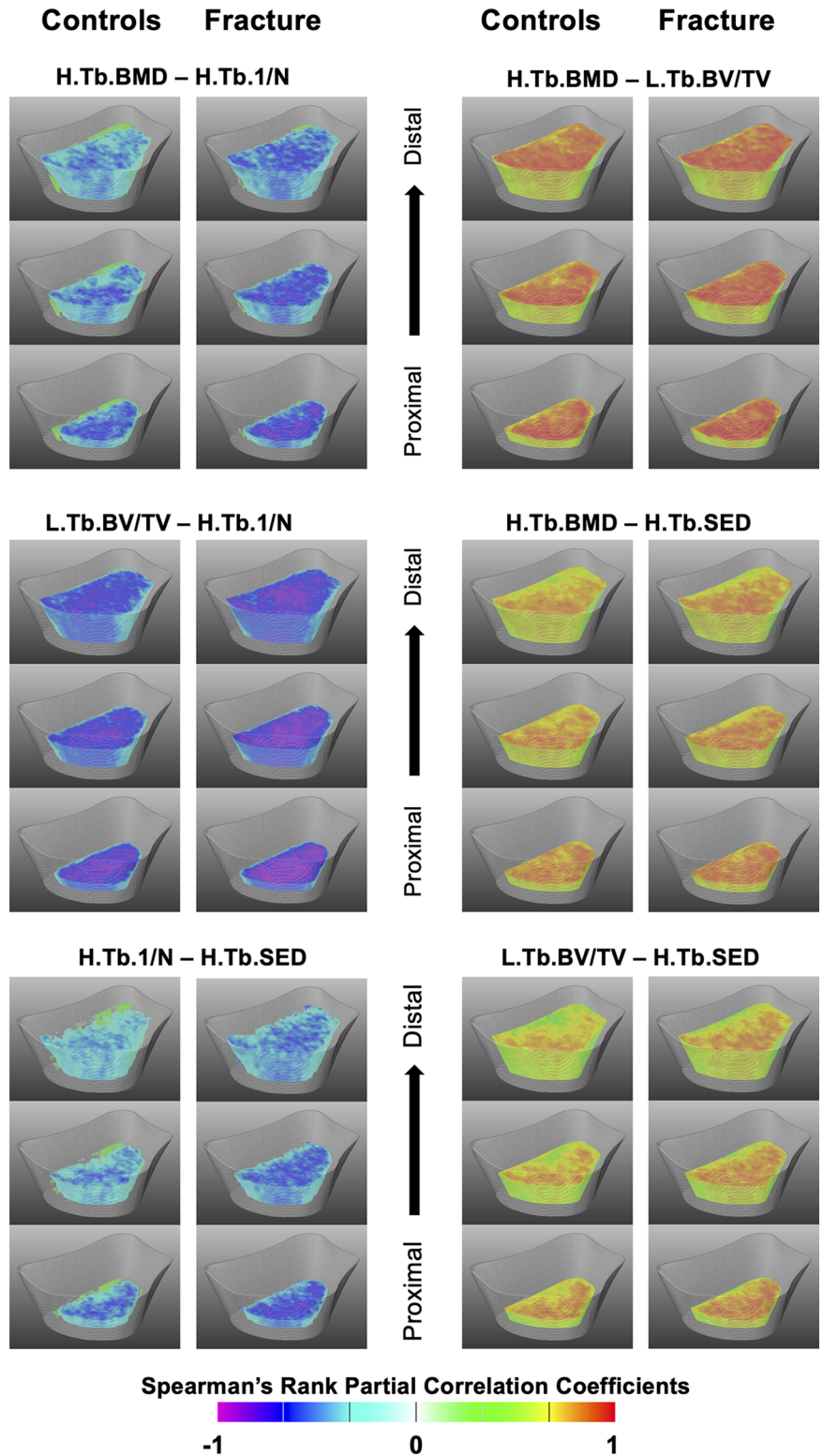
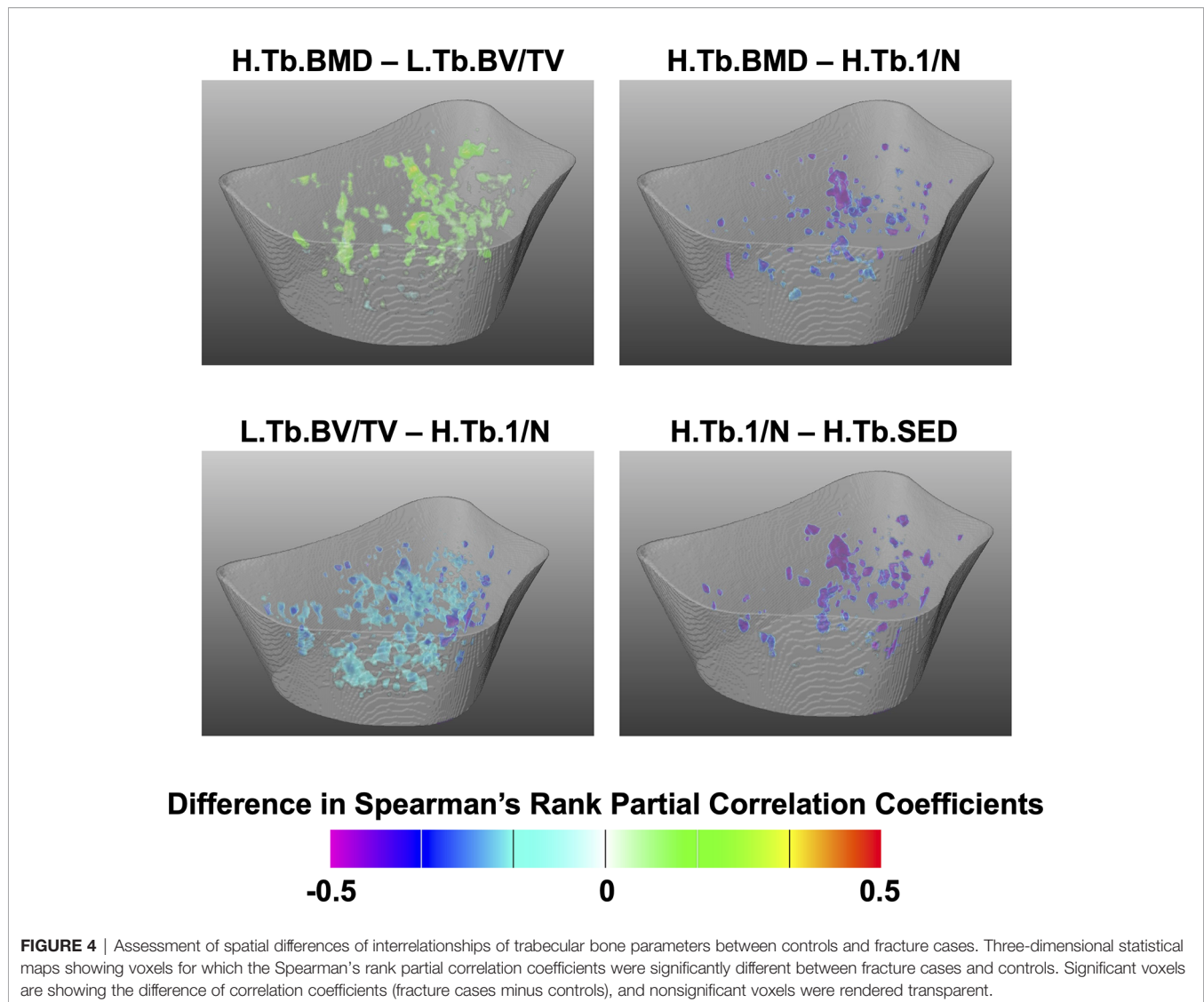


FIGURE 3 | Spatial assessment of interrelationships of trabecular bone parameters. Three-dimensional views at three different levels (1/4, 1/2 and 3/4 of the scan length) of the statistical maps showing Spearman's rank partial correlation coefficients for the different interrelationships of trabecular bone parameters for controls and fracture cases. All maps were adjusted for age, height, weight, and shape. Voxels that were no significant after correcting for multiple comparisons were rendered transparent.

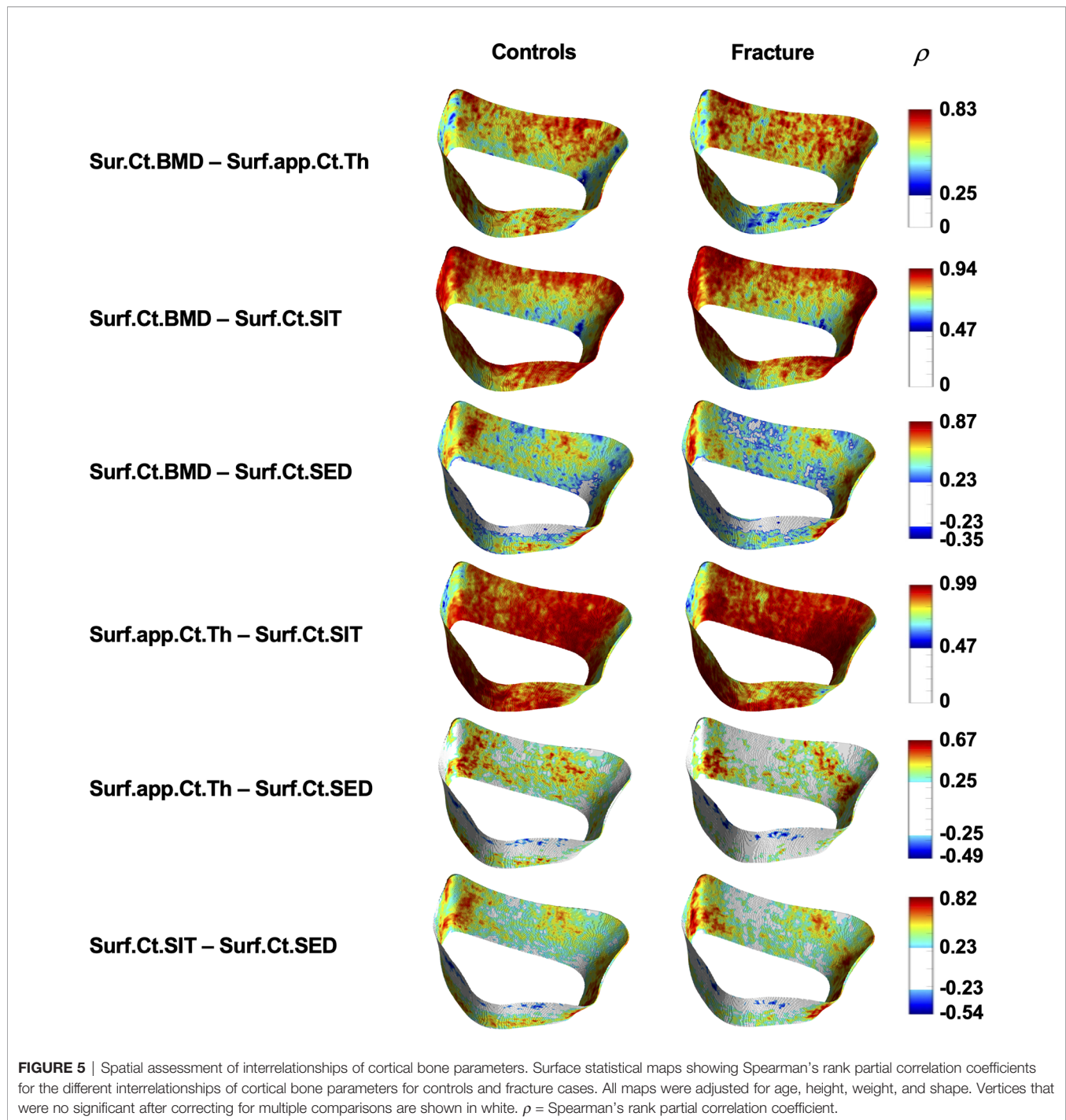


between controls and fracture cases were identified, particularly for trabecular bone, with stronger interrelationships in the fracture cases.

As previously reported by Melton et al. (18) and in agreement with previous cross-sectional studies (12, 16, 19), we found that the fracture cases had lower BMD, deterioration of bone microstructure and geometry, and lower μ FEA-derived bone strength compared with controls using the standard analysis techniques provided by the manufacturer (**Table 2**). Similar trends were observed for the global analyses of homogenized and local trabecular bone parameters, as well as for the surface-based assessments of cortical bone with no spatial normalization (**Table 4**). However, in contrast to H.Tb.SED, for which fracture cases showed significantly lower values than controls, Surf.Ct.SED was not significantly different between the two groups. This result is consistent with the original study of Melton et al. using the standard analysis method (18). SED represents the area under the stress-strain curve (31, 32) and

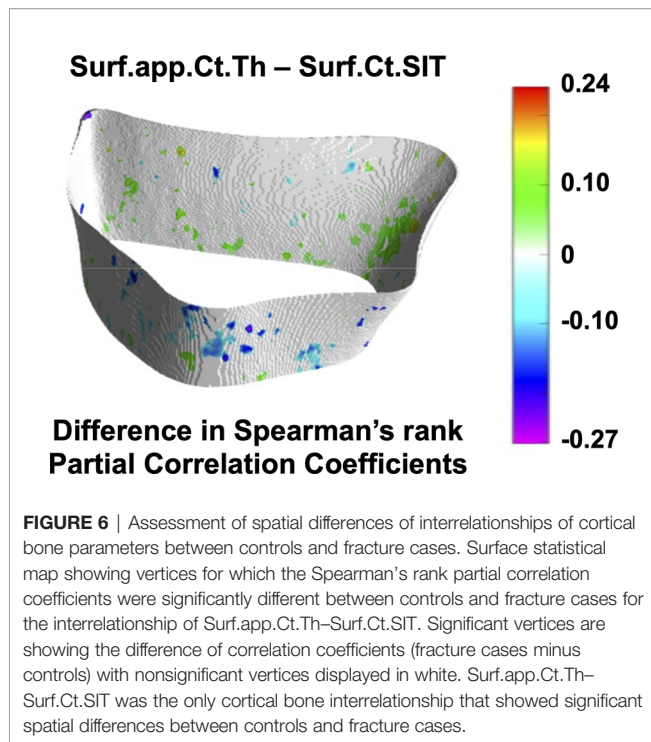
reflects the local energy stored per unit volume under the apparent load; therefore, our results suggest that the resistance to fracture in the cortical bone was maintained to some extent even in the fracture group. The lack of a significant difference in Surf.Ct.SED may be explained by compensatory prevention mechanisms of cortical deterioration (16) or to the axial load configuration of the μ FEA, which does not fully resemble fall-loading conditions. This result may be also partly attributed to the fact that the radius is an unloaded site.

Despite global differences in trabecular and cortical bone parameters between controls and fracture cases, results showed expected global significant correlations of bone density, microstructure, geometry and biomechanics for both the trabecular and the cortical compartments within each group, for both analysis methods (**Tables 3 and 5**). Our results are in agreement with those of Boutroy et al., who also reported significant expected interrelationships between density and microstructural parameters at the distal radius in



postmenopausal women using HR-pQCT (15). In that study, the trabecular correlations were in the absolute range of 0.78–0.91, while the correlation of Ct.BMD with Ct.Th was equal to 0.95. Here, the trabecular correlations between density and microstructural parameters were in the absolute range of 0.83–0.99, with the correlation of Ct.BMD and Ct.Th equal to 0.69 and 0.63 for controls and fracture cases, respectively. Our results also demonstrated significant correlations of density,

microstructure and geometry with biomechanical parameters derived from μ FEA ($|\rho| = 0.40$ – 0.67). Moreover, we identified significant heterogeneous spatial distributions of interrelationships of bone parameters across the distal radius for both the trabecular (Figure 3) and the cortical bone compartments (Figure 5) within each group. In particular, both groups manifested stronger Spearman's rank partial correlations proximally than distally for most of the



trabecular interrelationships; with an opposite trend for the cortical interrelationships of Surf.Ct.BMD with Surf.app.Ct.Th and Surf.Ct.SIT, i.e., stronger correlations distally than proximally for both groups. These observations might be partly explained by the study of Boyd (33), who showed an increase in Tb.N and a decrease in Ct.Th from the proximal to the distal end of the radius. Interestingly, the local interrelationships of Surf.Ct.SED with other cortical parameters were in general small, even to the point of showing nonsignificant areas on the distal end for both groups. Another interesting finding for SED, was that for the trabecular compartment the correlations were in general stronger in the dorsal side, while for the cortical compartment they were stronger in the palmar side in both groups. Although previous studies have demonstrated regional

structural variations of trabecular and cortical bone (34, 35), the regions in those studies were predefined, limiting the local assessments to the size and location of those regions. Here, by using our statistical parametric mapping (SPM) framework for HR-pQCT studies (28), comprehensive local assessments of interrelationships of bone parameters were possible across the distal radius in both the trabecular and cortical compartments. Nevertheless, results of this study and those based on predefined regions of interest (34–36) underscore the relevance of local assessments parallel to the global analyses to improve our understanding of bone strength.

Although we identified significant global and local interrelationships between all bone parameters within each group, and even similar heterogeneous spatial distributions of the correlation coefficients between groups, the results showed significant different global (Tables 3 and 5) and local interrelationships (Figures 4 and 6) between groups. In terms of cortical bone, there were no significant differences between groups using the standard analysis techniques (Table 3). However, the compartmental interrelationships of Surf.Ct.SED with Surf.Ct.BMD and Surf.Ct.SIT showed significant differences between groups using surface-based assessments (Table 5). In addition, the Surf.app.Ct.Th–Surf.Ct.SIT partial correlation coefficient maps yielded small clusters of significant correlation differences between groups (Figure 6). The differences in the compartmental interrelationships of Surf.Ct.SED might be indicators of compensatory mechanisms in the cortical bone to maintain bone strength in the fracture group. The spatial differences in the Surf.app.Ct.Th–Surf.Ct.SIT correlations between groups were probably due to cortical porosity which is taken into account by Surf.Ct.SIT. In terms of trabecular bone, the partial correlations of H.Tb.BMD–L.Tb.BV/TV, H.Tb.BMD–H.Tb.1/N, and L.Tb.BV/TV–H.Tb.1/N were significantly different between groups both at the global (Table 5) and local level (Figure 4), although only the interrelationship of Tb.BMD–Tb.N was significantly different between groups using the standard analysis method (Table 3). In addition, small clusters of significant correlation differences between groups were observed for H.Tb.1/N–H.Tb.SED (Figure 4). This correlation was not significantly different between groups at the compartmental level (Table 5).

TABLE 4 | Homogenized and local trabecular voxel-based parameters, and cortical surface-based parameters with no spatial normalization.

Parameter	Controls	Fracture cases	p-values
H.Tb.BMD (mg/cm ³)	354.2 ± 37.0	332.5 ± 35.5	<0.001*
L.Tb.BV/TV	0.22 ± 0.05	0.19 ± 0.05	<0.001*
H.Tb.1/N (voxels)	7.92 ± 3.40	8.91 ± 2.87	0.020*
H.Tb.SED (J/mm ³)	0.08 ± 0.03	0.06 ± 0.03	<0.001*
Surf.Ct.BMD (mg/cm ³)	830.6 ± 91.5	793.5 ± 91.2	<0.001*
Surf.app.Ct.Th (mm)	0.98 ± 0.17	0.91 ± 0.15	<0.001*
Surf.Ct.SIT (mm)	0.72 ± 0.14	0.66 ± 0.12	<0.001*
Surf.Ct.SED (J/mm ³)	0.27 ± 0.03	0.26 ± 0.03	NS

Values are shown as mean ± standard deviation.

Linear regression adjusting for age, height, and weight.

*Significant at $p < 0.05$.

NS = $P \geq 0.05$.

TABLE 5 | Global compartmental Spearman's rank partial correlations for homogenized and local trabecular voxel-based parameters, and for cortical surface-based parameters with no spatial normalization.

Interrelationships		Controls		Fracture cases		Controls vs. Fracture cases
		ρ	<i>p</i> -value	ρ	<i>p</i> -value	<i>p</i> -value
H.Tb.BMD	L.Tb.BV/TV	0.83	<0.001*	0.93	<0.001*	0.003*
H.Tb.BMD	H.Tb.1/N	-0.44	<0.001*	-0.75	<0.001*	0.001*
H.Tb.BMD	H.Tb.SED	0.78	<0.001*	0.65	<0.001*	NS
L.Tb.BV/TV	H.Tb.1/N	-0.82	<0.001*	-0.91	<0.001*	0.015*
L.Tb.BV/TV	H.Tb.SED	0.64	<0.001*	0.62	<0.001*	NS
H.Tb.1/N	H.Tb.SED	-0.28	0.006*	-0.44	<0.001*	NS
Surf.Ct.BMD	Surf.app.Ct.Th	0.82	<0.001*	0.77	<0.001*	NS
Surf.Ct.BMD	Surf.Ct.SIT	0.86	<0.001*	0.83	<0.001*	NS
Surf.Ct.BMD	Surf.Ct.SED	0.80	<0.001*	0.59	<0.001*	0.004*
Surf.app.Ct.Th	Surf.Ct.SIT	0.99	<0.001*	0.99	<0.001*	NS
Surf.app.Ct.Th	Surf.Ct.SED	0.61	<0.001*	0.40	<0.001*	NS
Surf.Ct.SIT	Surf.Ct.SED	0.66	<0.001*	0.45	<0.001*	0.046*

ρ = Spearman's rank partial correlation coefficient.

Spearman's rank partial correlations were adjusted for age, height and weight.

The Fisher's Z transformation was used to compare correlation coefficients between groups.

*Significant at $p < 0.05$.

NS = $P \geq 0.05$.

TABLE 6 | Global compartmental Spearman's rank partial correlations of μ FEA.FL with homogenized and local trabecular voxel-based parameters, and cortical surface-based parameters with no spatial normalization.

Interrelationships		Controls		Fracture cases		Controls vs. Fracture cases
		ρ	<i>p</i> -value	ρ	<i>p</i> -value	<i>p</i> -value
H.Tb.BMD		0.76	<0.001*	0.68	<0.001*	NS
L.Tb.BV/TV		0.71	<0.001*	0.67	<0.001*	NS
H.Tb.1/N		-0.45	<0.001*	-0.59	<0.001*	NS
H.Tb.SED		0.67	<0.001*	0.57	<0.001*	NS
Surf.Ct.BMD		0.52	<0.001*	0.46	<0.001*	NS
Surf.app.Ct.Th		0.69	<0.001*	0.75	<0.001*	NS
Surf.Ct.SIT		0.68	<0.001*	0.72	<0.001*	NS
Surf.Ct.SED		0.28	0.005*	0.17	NS	NS

ρ = Spearman's rank partial correlation coefficient.

Spearman's rank partial correlations were adjusted for age, height and weight.

The Fisher's Z transformation was used to compare correlation coefficients between groups.

*Significant at $p < 0.05$.

NS = $P \geq 0.05$.

An interesting finding was that in the significant global and local correlation differences in the trabecular bone, fracture cases showed stronger correlation coefficients than controls. The opposite effect was observed for cortical bone, i.e., in the significant global and local correlation differences, controls showed stronger correlation coefficients than the fracture cases. These compartmental differences in the strength of the correlations between controls and fracture cases indicate that postmenopausal women with a recent Colles' fracture might undergo a synergistic decline in bone quantity and quality in the trabecular bone compartment, with a differential response of bone properties in the cortical compartment, effectively affecting compartmental bone biomechanics as was observed with SED (Table 4).

In agreement with previous studies, our results suggest that assessment of the trabecular bone in the distal radius might yield parameters that are more sensitive to prevent fragility fractures

(6, 7), including Colles' fracture (16). In fact, a previous HR-pQCT study demonstrated that trabecular bone microstructure at baseline is important to predict the risk of fracture in postmenopausal women with denosumab treatment (37). Therefore, our results may indicate that the loss of both BMD and bone quality on the trabecular compartment is likely to be strongly associated with fragility fractures.

This study has two main limitations. First, Colles' fractures occurred with a median of 7 months prior to the HR-pQCT scans, i.e., this is not a prospective study, which limits to certain extent the impact of our findings. Second, the unaffected side had to be scanned for the fracture group, which might not fully represent the affected side since a previous study demonstrated side-to-side differences of cortical area and failure load at the radius of healthy women (38). However, in the same study, no significant differences regarding other cortical and trabecular parameters were reported.

In conclusion, we assessed global and spatial interrelationships of bone density, microstructure, geometry, and biomechanics in postmenopausal women with and without a Colles' fracture, as well as the global and spatial differences of these interrelationships between the control and fracture groups. We showed significant heterogeneous spatial distributions of these interrelationships across the distal radius within each group, and also found small clusters of significant differences for these interrelationships between groups, particularly in the trabecular bone compartment. Our findings indicate that local bone properties of BMD, microstructure, and geometry are heterogeneous in the distal radius, and that trabecular bone parameters may play a major role in the assessment of bone fragility at this anatomical site.

DATA AVAILABILITY STATEMENT

The data analyzed in this study is subject to the following licenses/restrictions: The HR-pQCT images are owned by

Mayo Clinic. Requests to access these datasets should be directed to principal investigator SK.

AUTHOR CONTRIBUTIONS

KS: Analysis and interpretation of data, manuscript drafting, and revision. AB: Conception and design, interpretation of data, and manuscript revision. MO: Interpretation of data and manuscript revision. SK: Principal investigator of the original Colles' fracture study, interpretation of data, and manuscript revision. JC-G: Conception and design, analysis and interpretation of data, manuscript drafting and revision. All authors contributed to the article and approved the submitted version.

FUNDING

This work was supported in part by NIH R01AR068456 and NIH R01AR027065.

REFERENCES

- Consensus. conference. Osteoporosis Prevention, Diagnosis, and Therapy. *JAMA* (2001) 285(6):785–95. doi: 10.1001/jama.285.6.785
- Curtis EM, Moon RJ, Harvey NC, Cooper C. The Impact of Fragility Fracture and Approaches to Osteoporosis Risk Assessment Worldwide. *Bone* (2017) 104(11):29–8. doi: 10.1016/j.bone.2017.01.024
- Schuit SCE, Van Der Klift M, Weel AEAM, De Laet CEDH, Burger H, Seeman E, et al. Fracture Incidence and Association With Bone Mineral Density in Elderly Men and Women: The Rotterdam Study. *Bone* (2004) 34(1):195–202. doi: 10.1016/j.bone.2003.10.001
- Cranney A, Jamal SA, Tsang JF, Josse RG, Leslie WD. Low Bone Mineral Density and Fracture Burden in Postmenopausal Women. *Cmaj* (2007) 177(6):575–80. doi: 10.1503/cmaj.070234
- Biver E, Durosier-Izart C, Chevalley T, van Rietbergen B, Rizzoli R, Ferrari S. Evaluation of Radius Microstructure and Areal Bone Mineral Density Improves Fracture Prediction in Postmenopausal Women. *J Bone Miner Res* (2018) 33(2):328–37. doi: 10.1002/jbmr.3299
- Burt LA, Manske SL, Hanley DA, Boyd SK. Lower Bone Density, Impaired Microarchitecture, and Strength Predict Future Fragility Fracture in Postmenopausal Women: 5-Year Follow-up of the Calgary CaMos Cohort. *J Bone Miner Res* (2018) 33(4):589–97. doi: 10.1002/jbmr.3347
- Sornay-Rendu E, Boutroy S, Duboeuf F, Chapurlat RD. Bone Microarchitecture Assessed by HR-pQCT as Predictor of Fracture Risk in Postmenopausal Women: The OFELY Study. *J Bone Miner Res* (2017) 32(6):1243–51. doi: 10.1002/jbmr.3105
- Langsetmo L, Peters KW, Burghardt AJ, Ensrud KE, Fink HA, Cawthon PM, et al. Volumetric Bone Mineral Density and Failure Load of Distal Limbs Predict Incident Clinical Fracture Independent HR-pQCT BMD and Failure Load Predicts Incident Clinical Fracture of FRAX and Clinical Risk Factors Among Older Men. *J Bone Miner Res* (2018) 33(7):1302–11. doi: 10.1002/jbmr.3433
- Burghardt AJ, Link TM, Majumdar S. High-Resolution Computed Tomography for Clinical Imaging of Bone Microarchitecture. *Clin Orthop Relat Res* (2011) 469(8):2179–93. doi: 10.1007/s11999-010-1766-x
- Nishiyama KK, Shane E. Clinical Imaging of Bone Microarchitecture With HR-pQCT. *Curr Osteoporosis Rep* (2013) 11(2):147–55. doi: 10.1007/s11914-013-0142-7
- Vilaythiou N, Boutroy S, Sornay-rendu E, Van rietbergen B, Munoz F, Delmas PD, et al. Finite Element Analysis Performed on Radius and Tibia HR-pQCT Images and Fragility Fractures at All Sites in Postmenopausal Women. *Bone* (2010) 46(4):1030–7. doi: 10.1016/j.bone.2009.12.015
- Boutroy S, Van Rietbergen B, Sornay-Rendu E, Munoz F, Bouxsein ML, Delmas PD. Finite Element Analysis Based on In Vivo HR-pQCT Images of the Distal Radius Is Associated With Wrist Fracture in Postmenopausal Women. *J Bone Miner Res* (2008) 23(3):392–9. doi: 10.1359/JBMR.071108
- Lespessailles E, Ibrahim-Nasser N, Toumi H, Chapurlat R. Contribution of High Resolution Peripheral Quantitative CT to the Management of Bone and Joint Diseases. *Joint Bone Spine* (2018) 85(3):301–6. doi: 10.1016/j.jbspin.2017.04.012
- Hung LK, Wu HT, Leung PC, Qin L. Low BMD is a Risk Factor for Low-Energy Colles' Fractures in Women Before and After Menopause. *Clin Orthop Relat Res* (2005) 435:219–25. doi: 10.1097/01.blo.0000155345.04782.14
- Boutroy S, Bouxsein ML, Munoz F, Delmas PD. In Vivo Assessment of Trabecular Bone Microarchitecture by High-Resolution Peripheral Quantitative Computed Tomography. *J Clin Endocrinol Metab* (2005) 90(12):6508–15. doi: 10.1210/jc.2005-1258
- Vico L, Zouch M, Amirouche A, Frère D, Laroche N, Koller B, et al. High-Resolution pQCT Analysis at the Distal Radius and Tibia Discriminates Patients With Recent Wrist and Femoral Neck Fractures. *J Bone Miner Res* (2008) 23(11):1741–50. doi: 10.1359/jbmr.080704
- Sornay-Rendu E, Boutroy S, Munoz F, Delmas PD. Alterations of Cortical and Trabecular Architecture Are Associated With Fractures in Postmenopausal Women, Partially Independent of Decreased BMD Measured by DXA: The OFELY Study. *J Bone Miner Res* (2007) 22(3):425–33. doi: 10.1359/jbmr.061206
- Melton LJ, Christen D, Riggs BL, Achenbach SJ, Müller R, Van Lenthe GH, et al. Assessing Forearm Fracture Risk in Postmenopausal Women. *Osteoporosis Int* (2010) 21(7):1161–9. doi: 10.1007/s00198-009-1047-2
- Melton LJ, Riggs BL, Van Lenthe GH, Achenbach SJ, Müller R, Bouxsein ML, et al. Contribution of In Vivo Structural Measurements and Load/Strength Ratios to the Determination of Forearm Fracture Risk in Postmenopausal Women. *J Bone Miner Res* (2007) 22(9):1442–8. doi: 10.1359/jbmr.070514
- Palvanen M, Kannus P, Parkkari J, Pitkääjärvi T, Pasanen M, Vuori I, et al. The Injury Mechanisms of Osteoporotic Upper Extremity Fractures Among Older Adults: A Controlled Study of 287 Consecutive Patients and Their 108 Controls. *Osteoporosis Int* (2000) 11(10):822–31. doi: 10.1007/s001980070040
- Pialat JB, Burghardt AJ, Sode M, Link TM, Majumdar S. Visual Grading of Motion Induced Image Degradation in High Resolution Peripheral Computed Tomography: Impact of Image Quality on Measures of Bone Density and Micro-Architecture. *Bone* (2012) 50(1):111–8. doi: 10.1016/j.bone.2011.10.003

22. Tjong W, Kazakia GJ, Burghardt AJ, Majumdar S. The Effect of Voxel Size on High-Resolution Peripheral Computed Tomography Measurements of Trabecular and Cortical Bone Microstructure. *Med Phys* (2012) 39(4):1893–903. doi: 10.1118/1.3689813
23. Kazakia GJ, Hyun B, Burghardt AJ, Krug R, Newitt DC, De Papp AE, et al. In Vivo Determination of Bone Structure in Postmenopausal Women: A Comparison of HR-pQCT and High-Field MR Imaging. *J Bone Miner Res* (2008) 23(4):463–74. doi: 10.1359/jbmr.071116
24. Burghardt AJ, Buie HR, Laib A, Majumdar S, Boyd SK. Reproducibility of Direct Quantitative Measures of Cortical Bone Microarchitecture of the Distal Radius and Tibia by HR-pQCT. *Bone* (2010) 47(3):519–28. doi: 10.1016/j.bone.2010.05.034
25. Laib A, Hauselmann HJ, Rueggsegger P. In Vivo High Resolution 3D-QCT of the Human Forearm. *Technol Health Care* (1998) 6(5–6):329–37. doi: 10.3233/thc-1998-65-606
26. Bouxsein ML, Boyd SK, Christiansen BA, Guldberg RE, Jepsen KJ, Müller R. Guidelines for Assessment of Bone Microstructure in Rodents Using Micro-Computed Tomography. *J Bone Miner Res* (2010) 25(7):1468–86. doi: 10.1002/jbmr.141
27. Mueller TL, Christen D, Sandercott S, Boyd SK, van Rietbergen B, Eckstein F, et al. Computational Finite Element Bone Mechanics Accurately Predicts Mechanical Competence in the Human Radius of an Elderly Population. *Bone* (2011) 48(6):1232–8. doi: 10.1016/j.bone.2011.02.022
28. Carballido-Gamio J, Bonaretti S, Kazakia GJ, Khosla S, Majumdar S, Lang TF, et al. Statistical Parametric Mapping of HR-pQCT Images: A Tool for Population-Based Local Comparisons of Micro-Scale Bone Features. *Ann Biomed Eng* (2017) 45(4):949–62. doi: 10.1007/s10439-016-1754-8
29. Krebs A, Graeff C, Frieling I, Kurz B, Timm W, Engelke K, et al. High Resolution Computed Tomography of the Vertebrae Yields Accurate Information on Trabecular Distances If Processed by 3D Fuzzy Segmentation Approaches. *Bone* (2009) 44(1):145–52. doi: 10.1016/j.bone.2008.08.131
30. Genovese CR, Lazar NA, Nichols T. Thresholding of Statistical Maps in Functional Neuroimaging Using the False Discovery Rate. *NeuroImage* (2002) 15(4):870–8. doi: 10.1006/nimg.2001.1037
31. Hart NH, Nimphius S, Rantalainen T, Ireland A, Sifariakas A, Newton RU. Mechanical Basis of Bone Strength: Influence of Bone Material, Bone Structure and Muscle Action. *J Musculoskelet Neuronal Interact* (2017) 17(3):114–39.
32. Burghardt AJ, Kazakia GJ, Ramachandran S, Link TM, Majumdar S. Age- and Gender-Related Differences in the Geometric Properties and Biomechanical Significance of Intracortical Porosity in the Distal Radius and Tibia. *J Bone Miner Res* (2010) 25(5):983–93. doi: 10.1359/jbmr.091104
33. Boyd SK. Site-Specific Variation of Bone Micro-Architecture in the Distal Radius and Tibia. *J Clin Densitom* (2008) 11(3):424–30. doi: 10.1016/j.jocd.2007.12.013
34. Sode M, Burghardt AJ, Kazakia GJ, Link TM, Majumdar S. Regional Variations of Gender-Specific and Age-Related Differences in Trabecular Bone Structure of the Distal Radius and Tibia. *Bone* (2010) 46(6):1652–60. doi: 10.1016/j.bone.2010.02.021
35. Kazakia GJ, Nirody JA, Bernstein G, Sode M, Burghardt AJ, Majumdar S. Age- and Gender-Related Differences in Cortical Geometry and Microstructure: Improved Sensitivity by Regional Analysis. *Bone* (2013) 52(2):623–31. doi: 10.1016/j.bone.2012.10.031
36. Du J, Brooke-Wavell K, Paggiosi MA, Hartley C, Walsh JS, Silberschmidt VV, et al. Characterising Variability and Regional Correlations of Microstructure and Mechanical Competence of Human Tibial Trabecular Bone: An in-Vivo HR-pQCT Study. *Bone* (2019) 121(September 2018):139–48. doi: 10.1016/j.bone.2019.01.013
37. Butscheidt S, Rolvien T, Vettorazzi E, Frieling I. Trabecular Bone Microarchitecture Predicts Fragility Fractures in Postmenopausal Women on Denosumab Treatment. *Bone* (2018) 114(March):246–51. doi: 10.1016/j.bone.2018.06.022
38. Hildebrandt EM, Manske SL, Hanley DA, Boyd SK. Bilateral Asymmetry of Radius and Tibia Bone Macroarchitecture and Microarchitecture: A High-Resolution Peripheral Quantitative Computed Tomography Study. *J Clin Densitom* (2016) 19(2):250–4. doi: 10.1016/j.jocd.2015.02.005

Conflict of Interest: The authors declare that the research was conducted in the absence of any commercial or financial relationships that could be construed as a potential conflict of interest.

Copyright © 2021 Shiraishi, Burghardt, Osaki, Khosla and Carballido-Gamio. This is an open-access article distributed under the terms of the Creative Commons Attribution License (CC BY). The use, distribution or reproduction in other forums is permitted, provided the original author(s) and the copyright owner(s) are credited and that the original publication in this journal is cited, in accordance with accepted academic practice. No use, distribution or reproduction is permitted which does not comply with these terms.